

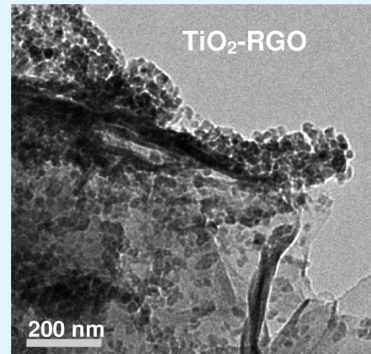
# Photocatalytic Synthesis of $\text{TiO}_2$ and Reduced Graphene Oxide Nanocomposite for Lithium Ion Battery

Jingxia Qiu, Peng Zhang, Min Ling, Sheng Li, Porun Liu, Huijun Zhao, and Shanqing Zhang\*

Centre for Clean Environment and Energy, Environmental Futures Centre, and Griffith School of Environment, Gold Coast Campus, Griffith University QLD 4222, Australia

**ABSTRACT:** In this work, we synthesized graphene oxide (GO) using the improved Hummers' oxidation method.  $\text{TiO}_2$  nanoparticles can be anchored on the GO sheets via the abundant oxygen-containing functional groups such as epoxy, hydroxyl, carbonyl, and carboxyl groups on the GO sheets. Using the  $\text{TiO}_2$  photocatalyst, the GO was photocatalytically reduced under UV illumination, leading to the production of  $\text{TiO}_2$ -reduced graphene oxide ( $\text{TiO}_2$ -RGO) nanocomposite. The as-prepared  $\text{TiO}_2$ ,  $\text{TiO}_2$ -GO, and  $\text{TiO}_2$ -RGO nanocomposite were used to fabricate lithium ion batteries (LIBs) as the active anode materials and their corresponding lithium ion insertion/extraction performance was evaluated. The resultant LIBs of the  $\text{TiO}_2$ -RGO nanocomposite possesses more stable cyclic performance, larger reversible capacity, and better rate capability, compared with that of the pure  $\text{TiO}_2$  and  $\text{TiO}_2$ -GO samples. The electrochemical and materials characterization suggest that the graphene network provides efficient pathways for electron transfer, and the  $\text{TiO}_2$  nanoparticles prevent the restacking of the graphene nanosheets, resulting in the improvement in both electric conductivity and specific capacity, respectively. This work suggests that the  $\text{TiO}_2$  based photocatalytic method could be a simple, low-cost, and efficient approach for large-scale production of anode materials for lithium ion batteries.

**KEYWORDS:** lithium ion batteries, UV photocatalysis,  $\text{TiO}_2$ , reduced graphene oxide



## 1. INTRODUCTION

Lithium ion batteries (LIBs) have been the dominant power source for a myriad of types of portable electronic devices<sup>1</sup> and potential power source for electric vehicles.<sup>2</sup> To enhance LIB performance, a variety of nanomaterials, including  $\text{TiO}_2$ ,<sup>3,4</sup> graphene,<sup>5–7</sup> and its composite,<sup>8,9</sup> has been researched as alternative electrode materials.

$\text{TiO}_2$  has been particularly attractive for large-scale energy storage, because  $\text{TiO}_2$  is an abundant, inexpensive, and environmentally benign material with various types of nanostructures available (e.g., nanotubes,<sup>10,11</sup> nanowires,<sup>12,13</sup> and nanosheets<sup>14</sup>). Also,  $\text{TiO}_2$  is structurally stable with a small volume change (<4%) during Li ion insertion/extraction processes and intrinsically safe by avoiding Li electrochemical deposition.<sup>15</sup> However, low electronic conductivity within the  $\text{TiO}_2$  network and relatively low theoretic capacity are still the main obstacles for their practical applications. In this regard, nanocomposite of  $\text{TiO}_2$  and nanostructured carbon materials may be an efficient way to tackle the problems.<sup>16,17</sup>

Among various nanostructured carbon materials, graphene is expected to be an excellent supporting material of the nanocomposite as anodes, because of its superior electronic conductivity, high surface-to-volume ratio, ultrathin thickness, structural flexibility, and chemical stability.<sup>2</sup> The graphene network provides efficient pathways for electron transfer. However, the layered graphene sheets can naturally stack into multilayers and thus lose the advantages of high surface area and intrinsic chemical and physical properties. Nanoparticles

such as  $\text{TiO}_2$ ,<sup>15,18</sup>  $\text{SnO}_2$ ,<sup>19,20</sup>  $\text{Co}_3\text{O}_4$ ,<sup>21</sup> and  $\text{Fe}_3\text{O}_4$ <sup>22</sup> anchored on the graphene sheets could potentially resolve the problem of graphene stacking.

The preparation of graphene using chemical method commonly involves the oxidation of graphite to produce graphene oxide (GO) and reduction of GO. Chemical oxidation method (e.g., the traditional Hummers' method) is probably the most economical way to prepare GO in large quantity from natural graphite.<sup>23</sup> Recently, an improved Hummers' method was proposed by Tour's group<sup>24</sup> for the large-scale production of GO. The proposed method shows significant advantages over the Hummers' method: it has much higher production yield, does not involve a large exothermal reaction or the production of toxic gas, produces a higher fraction of well-oxidized hydrophilic carbon material, and possesses a more regular structure.

During the chemical oxidation of graphite, oxygen-containing functional groups, such as epoxy, hydroxyl, carbonyl, and carboxyl, are introduced onto the graphene sheets, which interrupts graphitic lattice and reduces the conductivity.<sup>25</sup> In order to restore the conductivity of graphene, these functional groups are removed by chemical reduction methods, such as hydrazine,<sup>26</sup> UV-induced reduction<sup>25</sup> or thermal reduction,<sup>26</sup> sonolysis.<sup>27</sup>

**Received:** April 23, 2012

**Accepted:** June 27, 2012

**Published:** June 27, 2012

Kamat and co-workers reported that GO can be photocatalytically reduced by the  $\text{TiO}_2$  nanoparticles under the UV illumination.<sup>25</sup> Since the functional groups on the graphene sheet cannot be removed completely, the reduction product of GO is commonly referred as reduced graphene oxide (RGO). This method has the following advantages: (1) the extend of the photocatalytic reduction can be tuned on demand by controlling reaction time; (2) no toxic chemicals are involved in the reduction reaction; and, most importantly, (3)  $\text{TiO}_2$  particles can be readily dispersed and strongly bound onto the newly RGO sheets, forming  $\text{TiO}_2$ -RGO nanocomposite due to the remaining functional groups. Rose and co-workers<sup>28</sup> demonstrated that the photocurrent generated by the  $\text{TiO}_2$ -RGO nanocomposite electrode was enhanced remarkably (10-fold), compared to the pure  $\text{TiO}_2$  electrode, because of the enhanced conductivity.

In this work, inspired by the above findings, in order to improve both electric conductivity and specific capacity, we attempt to incorporate the  $\text{TiO}_2$  nanoparticles with graphene nanosheets without restacking of the graphene nanosheets. We synthesize GO using the improved Hummers' oxidation method and prepare the  $\text{TiO}_2$ -RGO nanocomposite via the UV-induced photocatalytic reduction route to reduce GO and anchor the  $\text{TiO}_2$  nanoparticles onto the RGO sheets simultaneously. The as-prepared nanocomposites were used for fabrication of electrodes for LIBs. It is the first time, to the best of our knowledge, UV-induced reduction method is applied to prepare the  $\text{TiO}_2$ -RGO nanocomposite as electrode material for LIBs. The performance of the resultant LIBs was evaluated systematically.

## 2. EXPERIMENTAL SECTION

**2.1. Synthesis Procedures.** *a. Preparation of GO.* GO was synthesized via the oxidation of graphite using the improved Hummers' method, the oxidation method proposed by Tour's group.<sup>24</sup> Briefly, 2 g graphite and 12 g  $\text{KMnO}_4$  were placed into a mixture of  $\text{H}_2\text{SO}_4/\text{H}_3\text{PO}_4$  (240:26.7 mL) under vigorous stirring in sequence. The resultant solution was continually stirred at 50 °C for 12 h. After the solution was cooled to room temperature, it was poured onto ice (ca. 280 mL) and mixed with 3 mL of 30%  $\text{H}_2\text{O}_2$ . The solution was centrifuged and washed with 30% HCl, deionized water and ethanol in order, and filtered with a 0.45- $\mu\text{m}$  PTFE membrane. The residue on the filter (i.e., GO) was dried overnight at room temperature.

*b. Preparation of Anatase  $\text{TiO}_2$ .* Anatase  $\text{TiO}_2$  nanoparticles were prepared according to our previous work.<sup>29</sup> Briefly, a mixture of 25 mL of titanium butoxide and 8 mL of propan-2-ol was added dropwise to 300 mL of a 0.1 M nitric acid solution under vigorous stirring, resulting in a slurry. The slurry was heated to 80 °C and stirred vigorously for 10 h to achieve peptization. The resulting colloid was then hydrothermally treated in an autoclave at 200 °C for 12 h. The colloidal suspension was then introduced into a rotary evaporator and evaporated to a final solid concentration of ca. 2% w/v with particle sizes ranging from 8 nm to 10 nm.

*c. Preparation of the  $\text{TiO}_2$ -RGO Nanocomposite.* As shown in Figure 1, a homogeneous  $\text{TiO}_2$ -GO suspension was first obtained by mixing a 0.04 g of GO in ethanol and 25 mL of anatase  $\text{TiO}_2$  solution (ca. 2% w/v) in an ultrasonic bath. The sample was then placed into a photoreaction station under the UV irradiation of a 1000-W xenon lamp and continuous stirring for 2–5 h. The infrared light was blocked by a UV-band-pass filter. The resultant solution were filtered and rinsed with deionized water three times. Finally, the residue solids on the filter membrane, i.e.,  $\text{TiO}_2$ -RGO nanocomposite, were dried in a vacuum oven at 60 °C for 12 h. Part of the  $\text{TiO}_2$ -GO suspension was dried and assembled in coin cells for comparison purposes, using the same procedures as the  $\text{TiO}_2$ -RGO.

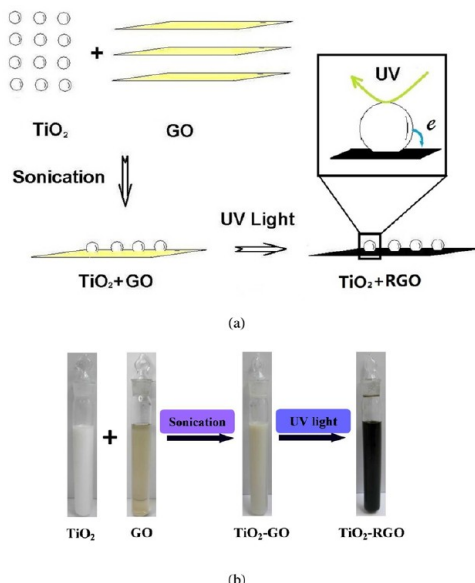


**Figure 1.** (a) Schematic diagram of the preparation of the  $\text{TiO}_2$ -RGO nanocomposite; (b) photographs of the products at different synthesis stages.

**2.2. Materials Characterization.** The microstructure and morphology of  $\text{TiO}_2$ -RGO were examined using transmission electron microscopy (TEM) (FEI Model Tecnai 20) with an acceleration voltage of 200 kV. XRD patterns were obtained on X-ray diffraction (XRD) (Model LabX-6000, Shimadzu, Japan) using  $\text{CuK}\alpha$  radiation at 40 kV and 40 mA over the  $2\theta$  range of 5–70 °C. The Raman spectra of  $\text{TiO}_2$ -RGO and GO were obtained using Raman spectroscopy (Jobin Yvon Model HR800).

**2.3. Electrode Preparation.** Active materials (i.e., the pure anatase  $\text{TiO}_2$ , the  $\text{TiO}_2$ -GO mixture, and  $\text{TiO}_2$ -RGO nanocomposite) were mixed with 10 wt % carbon black and 10 wt % poly(vinylidene fluoride) (PVDF, MW  $\approx$  534 000, Aldrich) in *N*-methyl-2-pyrrolidone (NMP, 99.5%, Aldrich) solvent to form a homogeneous slurry, respectively. The resultant slurries were uniformly coated onto Cu foils with an area of ca. 1  $\text{cm}^2$ . The weight of the active material is ca. 1–2 mg. All the pasted Cu foils, i.e., the anodes, were dried in a vacuum oven at 120 °C for 12 h and pressed using a double-roll compressor.

Using the anodes, CR2032 coin-type cells were assembled in an argon-filled M-Braun glovebox. A porous polypropylene film was used as the separator, a lithium sheet as the counter electrode, and 1 M  $\text{LiPF}_6$  in a 1:1 (w/w) mixture of ethylene carbonate (EC) and dimethyl carbonate (DMC) as the electrolyte. To measure the electrochemical capacity and cycle life of the working electrodes, the cells were galvanostatically charged and discharged using LAND-CT2001A battery tester (Wuhan, PRC) in a voltage range from 0.01 to 3.0 V vs  $\text{Li}/\text{Li}^+$  at the current densities of 100, 200, 400, 800, and 1600 mA/g, respectively.

Cyclic voltammograms (CVs) and electrochemical impedance spectroscopy (EIS) were performed using a CHI 660D electrochemical workstation (CH Instrument, Shanghai, PRC). CVs were recorded between 3.0 V and 0.0 V at a scan rate of 0.1 mV/s, using the composite as the working electrode and a lithium sheet as both counter electrode and reference electrode. AC impedance spectra were carried out with amplitude of 10 mV over the frequency range from 100 kHz to 0.01 Hz.

## 3. RESULTS AND DISCUSSION

**3.1. The Synthesis of  $\text{TiO}_2$ -RGO.** The GO used to prepare the  $\text{TiO}_2$ -RGO composite in this study was synthesized using the improved GO synthesis method.<sup>24</sup> In contrast to the traditional Hummers' method, this method can generate a larger amount of hydrophilic oxidized graphene material with

high production yield. We obtained 1.8 g of GO product from 1.0 g of graphite, which is close to the reported production yield.<sup>24</sup> Moreover, the reaction can be easily controlled and does not generate toxic gas.

The  $\text{TiO}_2$  colloid was freshly prepared by the hydrolysis of titanium butoxide.<sup>29</sup> It has a milky white color. The process of the UV induced reduction reaction is shown in Figure 1. When the  $\text{TiO}_2$  solution is ultrasonicated with GO, a stable and homogeneous  $\text{TiO}_2$ -GO mixture is obtained via the aforementioned interactions. The mixture has a light milky brown color (see Figure 1b). When the  $\text{TiO}_2$ -GO colloid is exposed to the UV light, the charge separation takes place and produces electron–hole pairs in  $\text{TiO}_2$  nanoparticles. The photoholes could easily capture the electrons from organic compounds (i.e., ethanol in this case). Under UV illumination, the electrons are continuously promoted to the conduction band at the surface of  $\text{TiO}_2$  surface.<sup>30</sup> The electrons are able to reduce the functional groups, including epoxy, hydroxyl, carbonyl, and carboxylic functional groups on the surface of GO sheets.<sup>25,31</sup> As a result, GO is converted into RGO, which is evidenced by the fact that the solution color changed from light brown (the color of  $\text{TiO}_2$ -GO) into black (the color of  $\text{TiO}_2$ -RGO) as shown in Figure 1b.<sup>25,28</sup> This anchoring of  $\text{TiO}_2$  nanoparticles onto RGO sheets could prevent the  $\text{TiO}_2$  nanoparticles from agglomeration and could minimize the restacking of RGO sheets, which will be beneficial to maintaining high surface areas and the stability of the nanocomposite during lithium insertion/extraction.

**3.2. Materials Characterization.** The structural composition of the graphite, as-prepared GO,  $\text{TiO}_2$  nanoparticles, and  $\text{TiO}_2$ -RGO nanocomposite were examined using XRD (Figure 2a). Before the oxidation reaction, the graphite showed a sharp and strong diffraction peak at  $2\theta = 26.4^\circ$  (see Figure 2a). After the oxidation reaction, the resultant GO shows a distinctive (002) peak at  $2\theta = 10.9^\circ$ ; this illustrates that most of the natural graphite was oxidized to GO and the *d*-spacing was expanded from 3.4 Å to 9.1 Å.<sup>24,32</sup> The  $\text{TiO}_2$ -RGO composites exhibits similar diffraction peaks corresponding to (101), (004), (200), (105), and (211) of pure anatase  $\text{TiO}_2$  particles. The diffraction peak for RGO was reported to appear at a  $2\theta$  angle of  $\sim 24.57^\circ$  (*d*-spacing  $\approx 3.62$  Å) and  $\sim 23^\circ$  (*d*-spacing  $\approx 3.86$  Å).<sup>33</sup> Interestingly, the XRD peaks corresponding to GO or RGO in the composite cannot be observed in Figure 2a. This phenomenon was attributed to the insufficient amount of carbon and relatively low diffraction intensity of the RGO in the literature.<sup>18</sup> In this work, this is more likely because the anchored  $\text{TiO}_2$  nanoparticles prevent the graphene sheets from restacking, substantially expand the *d*-spacing of the graphene layers, disrupt the layered and ordered structure, and consequently lead to the disappearance of the reflection peaks. This result also suggests the RGO sheets are effectively separated and highly dispersed into the  $\text{TiO}_2$  matrix.

In order to confirm the chemical composition of the composite, the Raman spectroscopy was used to characterize the RGO/ $\text{TiO}_2$  nanocomposite as well as the as-prepared GO (Figure 2b). According to the results examined by the thermogravimetric analysis (TGA), the as-prepared composite contains 5.6% (w/w) of RGO. In Raman spectra, both samples exhibit two strong peaks, denoted as the disorder peak (D, centered at  $1350\text{ cm}^{-1}$ ) and the graphitic peak (G, at  $\sim 1580\text{ cm}^{-1}$ ). The D peak suggests the disruption of the symmetrical hexagonal graphitic lattice, which associates with internal structure; and the G peak indicates the in-plane stretching

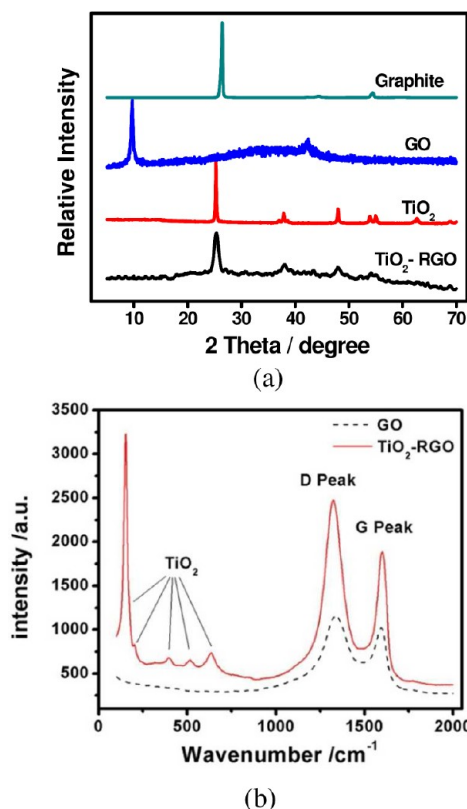


**Figure 2.** (a) XRD patterns of the graphite, GO, RGO,  $\text{TiO}_2$ , and  $\text{TiO}_2$ -RGO composites. (b) Raman spectra of the as-prepared GO and  $\text{TiO}_2$ -RGO.

motion of symmetric  $\text{sp}^2$  C–C bond.<sup>34</sup> Compared with the intensity ratio of  $I_D/I_G$  of GO (1.06), the ratio of the nanocomposite increased to 1.13, suggesting the decrease of the oxygen-functional groups on GO.<sup>35</sup> For  $\text{TiO}_2$ , due to  $E_g$  vibration modes of anatase, a sharp Raman scattering peak for free-standing anatase nanoparticles is commonly observed at  $143\text{ cm}^{-1}$ . In contrast, the peak was observed at  $153\text{ cm}^{-1}$ . The blue shift from  $143\text{ cm}^{-1}$  to  $153\text{ cm}^{-1}$  may be attributed to the interaction of RGO and  $\text{TiO}_2$ .<sup>36</sup> The peaks at  $\sim 195$ , 400, 516, and  $639\text{ cm}^{-1}$  correspond to the different vibration modes of anatase.<sup>37</sup> Overall, the Raman spectra suggest that the nanocomposite contains RGO and  $\text{TiO}_2$ , which is consistent with the XRD results.

To investigate the morphology and structure of the products, TEM and SEM images of the  $\text{TiO}_2$ -RGO composite were obtained as in Figure 3. The high-resolution TEM (HRTEM) image (see Figure 3b) indicates that the crystal lattice fringes with *d*-spacing of 0.352 nm corresponding to the (101) plane of the anatase  $\text{TiO}_2$ , which is consistent with the XRD results. The crystal lattice fringes of the RGO could not be observed by HRTEM, possibly because of their ultrathin structure.

Figure 3a shows that the  $\text{TiO}_2$  nanoparticles are well-dispersed and uniformly anchored on the surface of the RGO sheet. The SEM image (Figure 3c) of the  $\text{TiO}_2$ -RGO sample demonstrates the homogeneity of the composite in a large scale. In particular, only a small portion of RGO sheets and trace amount of freestanding  $\text{TiO}_2$  can be observed, while most of the RGO sheets are covered by the  $\text{TiO}_2$  nanoparticles (i.e., RGO-bonded  $\text{TiO}_2$ ). Also, majority of the  $\text{TiO}_2$  particles are anchored on the RGO sheets (with very small amount of freestanding  $\text{TiO}_2$  nanoparticles), which is very important, because

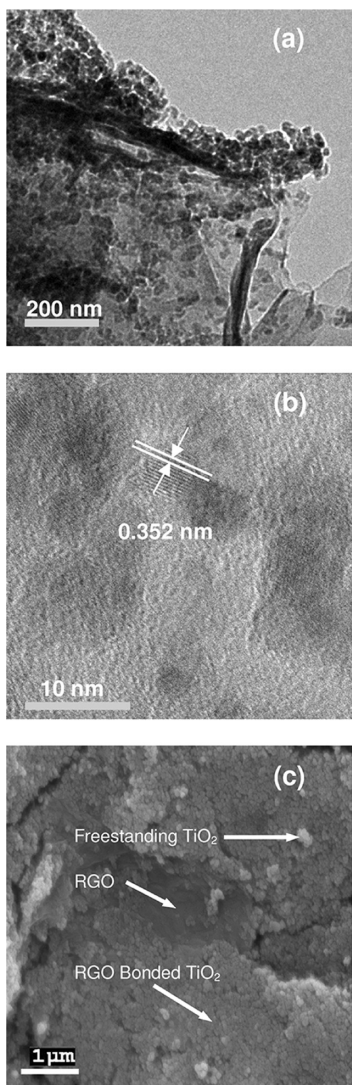


**Figure 3.** (a) TEM, (b) HRTEM, and (c) SEM images of the  $\text{TiO}_2$ -RGO nanocomposite.

this ensures the efficient electron collection via the RGO sheets during the insertion/extraction processes.

The formation mechanism of the  $\text{TiO}_2$ -RGO composite is proposed as follows. GO possesses oxygen-containing functional groups including epoxy, hydroxyl, carbonyl, and carboxyl functional groups. Epoxy and hydroxyl functional groups are the major part, existing on the basal plane of GO sheets, while carboxyl and carbonyl are the minor part, occurring on the edge of GO sheets.<sup>33,38</sup> Because  $\text{TiO}_2$  nanoparticles and its surface hydroxyl groups can readily interact with these functional groups,  $\text{TiO}_2$  nanoparticles can distribute uniformly on the surface of GO, which also facilitates the photocatalytic reduction of the GO. Under strong and prolonged UV illumination in the experiment, most of the oxygen-containing functional groups of GO are reduced and the  $\text{TiO}_2$  nanoparticles remain on the surface of RGO via electrostatic and/or van der Waals forces, resulting in the structure as shown in Figure 3a. It was reported that the interaction of RGO and  $\text{TiO}_2$  nanoparticles was attributed to the remaining carboxyl groups at the RGO and its strong adsorption to  $\text{TiO}_2$  nanoparticles.<sup>28</sup> This is different from our case, in that the carboxyl groups are mainly distributed on the edge of the GO

plane, while our  $\text{TiO}_2$  nanoparticles are scattered evenly on the RGO plane (see Figures 3a and 3c).

**3.3. Evaluation of Battery Performance.** It is well-established that the lithium ion insertion/extraction processes at anatase  $\text{TiO}_2$  nanoparticles proceed according to a reversible reaction:



The maximum value of  $x$  for a reversible reaction at room temperature is 0.5,<sup>39</sup> which corresponds to a capacity of 168 mAh/g. Usually, the voltage window for  $\text{TiO}_2$ -based anode materials is 1–3 V, because RGO contributes charge and discharge capacity under 1 V; we set the voltage window between 0.01 V to 3 V to obtain the full capacity of the composite. Figure 4 presents the charge/discharge profiles of

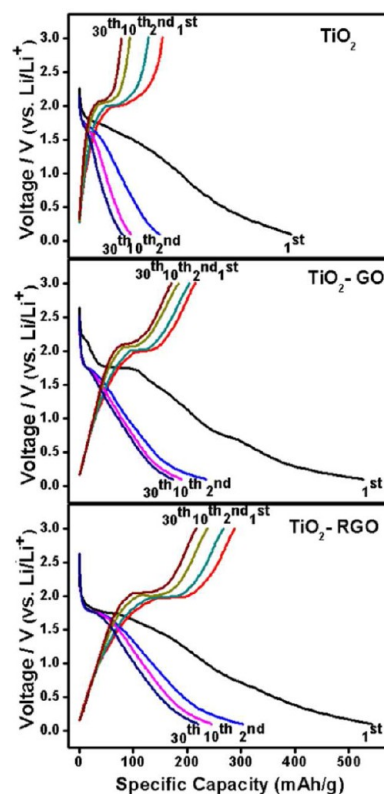


**Figure 4.** Galvanostatic charge–discharge curves of the  $\text{TiO}_2$ ,  $\text{TiO}_2$ -GO, and  $\text{TiO}_2$ -RGO cycled at 1st, 2nd, 10th, and 30th between 0.1 V and 3.0 V (vs  $\text{Li}/\text{Li}^+$ ) at a current density of 100 mA/g.

the  $\text{TiO}_2$ ,  $\text{TiO}_2$ -GO, and  $\text{TiO}_2$ -RGO composite electrode of the 1st, 2nd, 10th, and 30th cycles at a current density of 100 mA/g. The discharging plateaus at  $\sim 1.75$  V (insertion process) indicates the Li-intercalation into anatase  $\text{TiO}_2$  lattice and the charging plateaus observed at  $\sim 2.05$  V (extraction process) represented the Li-deintercalation of  $\text{Li}_x\text{TiO}_2$ .<sup>40</sup> The plateaus showed the typical electrochemical reaction of anatase  $\text{TiO}_2$  with lithium ions. The discharge curve showed a sloping plateau, followed by the  $\text{TiO}_2$  discharging plateau, which could be attributed to the electrochemical behavior of GO/RGO in the composites.

Interestingly, Figure 4 shows that the reversible specific capacity for  $\text{TiO}_2$ -RGO is  $\sim 310$  mAh/g, which is significantly higher than the theoretic capacity of  $\text{TiO}_2$  (168 mAh/g) and the theoretic capacity of the composite (200 mAh/g). The

theoretic capacity of the as-prepared composite is calculated based on fact that the composite contains 5.6% (w/w) RGO and 94.4% (w/w)  $\text{TiO}_2$  and the theoretical capacities are 168 and 744 mAh/g for  $\text{TiO}_2$  and graphene, respectively. This suggests that RGO could also contribute the specific capacity to the LIBs. This can be explained by the previous findings that the Li ion can be stored reversibly in the defects of the edge site and internal defects on RGO.<sup>41</sup> In the case of pure graphene, the Li-ion storage capacity in graphene could decrease rapidly, because of the restacking of the graphene nanosheets. In strong contrast, the restacking of the RGO sheets are effectively prevented by the anchored  $\text{TiO}_2$  particles as shown in the TEM image in Figure 3. Consequently, the reversibly capacity provided by the RGO are maintained.

In addition, the first discharge and charge capacities are, respectively, 395 and 160 mAh/g for the  $\text{TiO}_2$ , 536 and 220 mAh/g for the  $\text{TiO}_2$ -GO, and 546 and 296 mAh/g for the  $\text{TiO}_2$ -RGO. The  $\text{TiO}_2$ -RGO shows a higher Coulombic efficiency (54%) in the first cycle. In the case of the  $\text{TiO}_2$  and  $\text{TiO}_2$ -GO, in contrast, their Coulombic efficiency is lower (both ~40%), corresponding to a high irreversible capacity. The large initial capacity loss mainly results from the decomposition of electrolyte in the low-potential region and forming a passivation layer (solid electrolyte interface, SEI) on the surface of active materials. Nanostructured electrode materials normally possess better battery performance, in terms of cycle life, rate capability, specific capacity, and energy density, because of the much larger surface area. However, the large surface could lead to significant side reaction (i.e., decomposition of the electrolyte). In our case, the formation of the composite can effectively restrain the side reaction, which can be demonstrated by the fact that the Coulombic efficient of the composites sample was higher than that of the  $\text{TiO}_2$  and  $\text{TiO}_2$ -GO in the initial cycle.

We compare the electrochemical properties of the  $\text{TiO}_2$ -RGO composite, pure  $\text{TiO}_2$ , and  $\text{TiO}_2$ -GO, using 2032 coin-type cells to highlight the superiority of the  $\text{TiO}_2$ -RGO composite as anode material in LIBs. The cycling stabilities of the  $\text{TiO}_2$ -RGO nanocomposite, pure  $\text{TiO}_2$ , and  $\text{TiO}_2$ -GO are shown in Figure 5. The  $\text{TiO}_2$ -RGO sample shows great

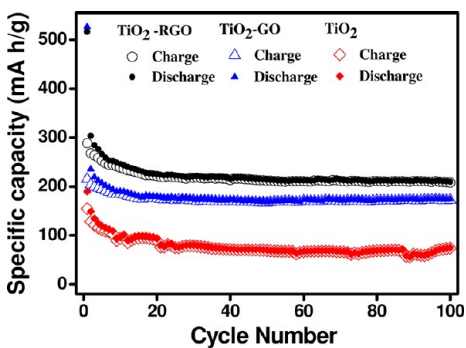


**Figure 5.** Specific capacities of the  $\text{TiO}_2$ ,  $\text{TiO}_2$ -GO, and  $\text{TiO}_2$ -RGO at a charge-discharge rate of 100 mA/g.

enhancement of the capacity retention in comparison with the pure  $\text{TiO}_2$  and  $\text{TiO}_2$ -GO samples. The reversible discharge and charge capacities are, respectively, 310 and 270 mAh/g for  $\text{TiO}_2$ -RGO, 220 and 161 mAh/g for  $\text{TiO}_2$ -GO, and 150 and 128 mAh/g for the  $\text{TiO}_2$ . Even up to 100 cycles, the  $\text{TiO}_2$ -RGO sample still preserves better electrochemical lithium storage performance (more than 200 mAh/g) than the  $\text{TiO}_2$  and  $\text{TiO}_2$ -GO.

GO electrodes. The improvement of the  $\text{TiO}_2$ -RGO, in terms of cycling stabilities, may be ascribed to the strong interaction between the  $\text{TiO}_2$  nanoparticles and RGO sheets.

Figure 6 shows the rate capabilities of  $\text{TiO}_2$ ,  $\text{TiO}_2$ -GO, and  $\text{TiO}_2$ -RGO at various current densities between 100 mA/g and

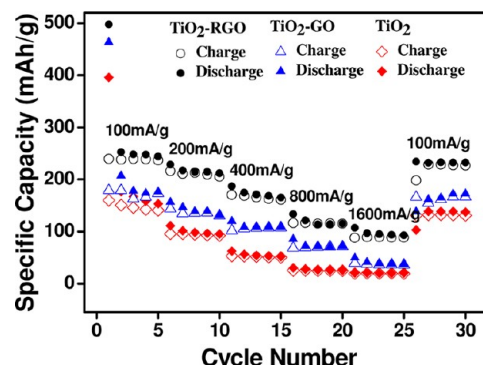


**Figure 6.** Rate capabilities of  $\text{TiO}_2$ ,  $\text{TiO}_2$ -GO, and  $\text{TiO}_2$ -RGO at various current densities.

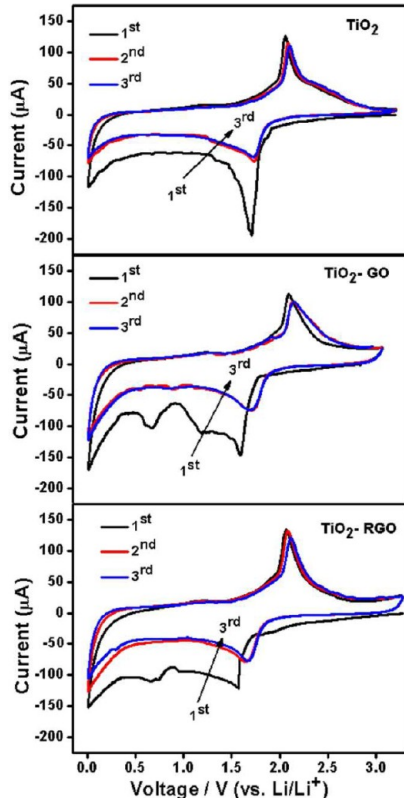
1600 mA/g. In particular, the reversible capacity of the composite sample is ~215 mAh/g at a current density of 200 mA/g. The cycling performance, in terms of the specific capacity, gradually declines with the increase of the current densities for all the samples. For example, at current densities of 800 and 1600 mA/g, the discharge capacity of the composite sample reduces to 160 and 100 mAh/g, respectively. In all cases, the  $\text{TiO}_2$ -RGO composite samples exhibits better rate capability, compared with the  $\text{TiO}_2$  and  $\text{TiO}_2$ -GO samples. Moreover, when the current density is set back to the initial 100 mA/g, the specific capacity of the  $\text{TiO}_2$ -RGO samples is fully recovered. This is beneficial from the strong bonding between the  $\text{TiO}_2$  nanoparticles and the RGO and rate capability contribution from RGO.

Table 1 shows the comparison of the electrochemical performance of the LIBs based on  $\text{TiO}_2$ -RGO or  $\text{TiO}_2$ -graphene composite composites in the literature. The as-prepared  $\text{TiO}_2$ -RGO is superior to some reported  $\text{TiO}_2$ /reduced graphene oxide or graphene, in terms of reversible capacity, and comparable with others, in terms of the rate capability in the literature.<sup>42,43</sup> The excellent electrochemical performance suggests that the photocatalytic reduction method is a simple, efficient approach for the preparation of  $\text{TiO}_2$ -RGO composite.

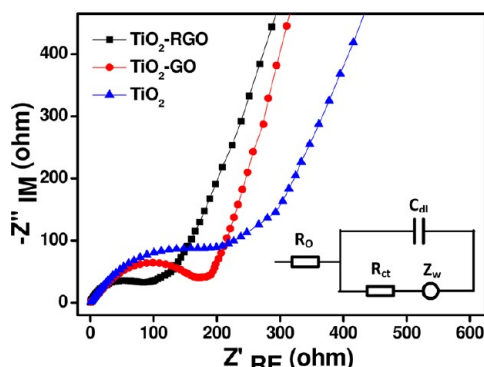
Lithium-ion insertion/extraction properties of the as-prepared electrodes were investigated using the CV technique (see Figure 7). In the first three cycles, all of the samples exhibit a pair of cathodic/anodic peaks at ~1.60 and 2.05 V, which can be ascribed to the Li-ion insertion/extraction in an anatase  $\text{TiO}_2$  lattice, respectively. The cathodic/anodic peaks are in accordance with the discharge/charge profiles in Figure 4. The upholding of the cathodic/anodic peak positions suggests that the reversibility of the  $\text{TiO}_2$  was well-maintained in the  $\text{TiO}_2$ -RGO composite. For the  $\text{TiO}_2$ -GO and  $\text{TiO}_2$ -RGO samples, we can observe that a prominent peak is located at ~0.6 V in the first cycle, because of the formation of SEI layer at the surface of the anodes. These peaks disappear during the subsequent cycle, because the SEI layer can isolate the anodes from the electrolyte, thereby preventing further decomposition of the electrolyte.

**Table 1. Comparison of the Electrochemical Performance of the As-Prepared  $\text{TiO}_2$ -RGO with Products Reported in the Literature**

material	preparing method	reversible capacity (mAh/g)	rate capability (mAh/g)	voltage window (V)	reference
anatase/RGO	photocatalytic reduction	310	100 @1600 mA/g	0.01–3.0	this work
anatase/RGO	hydrothermal	295.9	97.7 @2000 mA/g	0–3.0	43
graphene/ $\text{TiO}_2$	thermal reduction	~170	110 @10C	1.0–3.0	42

**Figure 7.** Cyclic voltammograms (CVs) of the  $\text{TiO}_2$ ,  $\text{TiO}_2$ -GO, and  $\text{TiO}_2$ -RGO at a scan rate of 0.1 mV/s.

AC impedance measurements are performed for all the samples at the charged state and the corresponding Nyquist plots are shown in Figure 8. The inset is the equivalent circuit, in which  $R_\Omega$  is the total resistance of the electrolyte, separator, and electrical contacts;  $R_{ct}$  is the charge-transfer resistance; and  $C_{dl}$  represents the double-layer resistance. In addition,  $Z_w$  is the Warburg impedance, reflecting the diffusion of Li ions. All the

**Figure 8.** Nyquist plots of the  $\text{TiO}_2$ ,  $\text{TiO}_2$ -GO, and  $\text{TiO}_2$ -RGO samples.

curves show similar characteristics, including a depressed semicircle in high and middle frequency range and an inclined line in the low frequency range, corresponding respectively to the charge-transfer resistance associated with the surface properties of insertion materials and the solid-state diffusion resistance of lithium ions within the host.<sup>44</sup> The ohmic resistances are calculated as 13, 8.5, 3.5 and the charge-transfer resistance are 280, 179, and 97 for  $\text{TiO}_2$ ,  $\text{TiO}_2$ -GO, and  $\text{TiO}_2$ -RGO, respectively. These results demonstrate that the conductivity of the graphene sheets was recovered by the  $\text{TiO}_2$  photocatalytic reduction of the oxygen-containing functional group on the GO sheets. Overall, the utilization of the RGO sheets facilitates the charge-transfer process in the LIBs.

## 4. CONCLUSIONS

The insufficient conductivity and theoretical capacity of  $\text{TiO}_2$  are the main drawbacks for practical application in Li-ion batteries. In this work, the  $\text{TiO}_2$ -reduced graphene oxide ( $\text{TiO}_2$ -RGO) nanocomposite was photocatalytically synthesized. The battery performance was significantly improved because of the unique combination of the  $\text{TiO}_2$  nanoparticles and the RGO sheets. On one hand, the conductivity of the  $\text{TiO}_2$ -RGO nanocomposite was enhanced by anchoring the  $\text{TiO}_2$  on the RGO sheets and removing the oxygen-containing functional groups, compared with that of corresponding the pure  $\text{TiO}_2$  and  $\text{TiO}_2$ -GO samples. On the other hand, the  $\text{TiO}_2$ -RGO sample exhibited much higher specific capacity than the pure  $\text{TiO}_2$  sample, because the RGO could also contribute specific capacity without the problem of graphene sheet restacking. This work suggests that the  $\text{TiO}_2$ -based photocatalytic method could be a simple, low-cost, and efficient approach for the large-scale production of anode materials for Li-ion batteries.

## ■ AUTHOR INFORMATION

### Corresponding Author

\*Tel.: 61-7-5552 8155. Fax: 61-7-5552 8067. E-mail: s.zhang@griffith.edu.au

### Notes

The authors declare no competing financial interest.

## ■ ACKNOWLEDGMENTS

The authors acknowledge the financial support of the ARC Discovery Grants from the Australian Research Council.

## ■ REFERENCES

- Chen, J. S.; Archer, L. A.; Lou, X. W. *J. Mater. Chem.* **2011**, *21*, 9912–9924.
- Etacheri, V.; Marom, R.; Elazari, R.; Salitra, G.; Aurbach, D. *Energy Environ. Sci.* **2011**, *4*, 3243–3262.
- Lafont, U.; Carta, D.; Mountjoy, G.; Chadwick, A. V.; Kelder, E. M. *J. Phys. Chem. C* **2009**, *114*, 1372–1378.
- Wang, J.; Zhou, Y.; Hu, Y.; O'Hare, R.; Shao, Z. *J. Phys. Chem. C* **2011**, *115*, 2529–2536.

(5) Xiao, X. C.; Liu, P.; Wang, J. S.; Verbrugge, M. W.; Balogh, M. P. *Electrochem. Commun.* **2011**, *13*, 209–212.

(6) Yoo, E.; Kim, J.; Hosono, E.; Zhou, H.-s.; Kudo, T.; Honma, I. *Nano Lett.* **2008**, *8*, 2277–2282.

(7) Guo, P.; Song, H. H.; Chen, X. H. *Electrochem. Commun.* **2009**, *11*, 1320–1324.

(8) Ding, S.; Chen, J. S.; Luan, D.; Boey, F. Y. C.; Madhavi, S.; Lou, X. W. *Chem. Commun.* **2011**, *47*, 5780.

(9) Shen, L.; Zhang, X.; Li, H.; Yuan, C.; Cao, G. *J. Phys. Chem. Lett.* **2011**, *2*, 3096–3101.

(10) Liu, D.; Zhang, Y.; Xiao, P.; Garcia, B. B.; Zhang, Q.; Zhou, X.; Jeong, Y.-H.; Cao, G. *Electrochim. Acta* **2009**, *54*, 6816–6820.

(11) Das, S. K.; Bhattacharyya, A. *J. J. Phys. Chem. C* **2009**, *113*, 17367–17371.

(12) Armstrong, G.; Armstrong, A. R.; Bruce, P. G.; Reale, P.; Scrosati, B. *Adv. Mater.* **2006**, *18*, 2597–2600.

(13) Wang, Y. F.; Wu, M. Y.; Zhang, W. F. *Electrochim. Acta* **2008**, *53*, 7863–7868.

(14) Chen, J. S.; Tan, Y. L.; Li, C. M.; Cheah, Y. L.; Luan, D.; Madhavi, S.; Boey, F. Y. C.; Archer, L. A.; Lou, X. W. *J. Am. Chem. Soc.* **2010**, *132*, 6124–6130.

(15) Wang, D.; Choi, D.; Li, J.; Yang, Z.; Nie, Z.; Kou, R.; Hu, D.; Wang, C.; Saraf, L. V.; Zhang, J.; Aksay, I. A.; Liu, J. *ACS Nano* **2009**, *3*, 907–914.

(16) Fu, L. J.; Liu, H.; Zhang, H. P.; Li, C.; Zhang, T.; Wu, Y. P.; Wu, H. Q. *J. Power Sources* **2006**, *159*, 219–222.

(17) Xu, J. W.; Wang, Y. F.; Li, Z. H.; Zhang, W. *J. Power Sources* **2008**, *175*, 903–908.

(18) Zhang, H.; Lv, X. J.; Li, Y. M.; Wang, Y.; Li, J. H. *ACS Nano* **2010**, *4*, 380–386.

(19) Li, Y.; Lv, X.; Lu, J.; Li, J. *J. Phys. Chem. C* **2010**, *114*, 21770–21774.

(20) Paek, S.-M.; Yoo, E.; Honma, I. *Nano Lett.* **2008**, *9*, 72–75.

(21) Wu, Z.-S.; Ren, W.; Wen, L.; Gao, L.; Zhao, J.; Chen, Z.; Zhou, G.; Li, F.; Cheng, H.-M. *ACS Nano* **2010**, *4*, 3187–3194.

(22) Li, B.; Cao, H.; Shao, J.; Qu, M.; Warner, J. H. *J. Mater. Chem.* **2011**, *21*, 5069–5075.

(23) Hummers, W. S.; Offeman, R. E. *J. Am. Chem. Soc.* **1958**, *80*, 1339–1339.

(24) Marcano, D. C.; Kosynkin, D. V.; Berlin, J. M.; Sinitskii, A.; Sun, Z.; Slesarev, A.; Alemany, L. B.; Lu, W.; Tour, J. M. *ACS Nano* **2010**, *4*, 4806–4814.

(25) Williams, G.; Seger, B.; Kamat, P. V. *ACS Nano* **2008**, *2*, 1487–1491.

(26) Gao, X.; Jang, J.; Nagase, S. *J. Phys. Chem. C* **2009**, *114*, 832–842.

(27) Vinodgopal, K.; Neppolian, B.; Lightcap, I. V.; Grieser, F.; Ashokkumar, M.; Kamat, P. V. *J. Phys. Chem. Lett.* **2010**, *1*, 1987–1993.

(28) Bell, N. J.; Yun, H. N.; Du, A. J.; Coster, H.; Smith, S. C.; Amal, R. *J. Phys. Chem. C* **2011**, *115*, 6004–6009.

(29) Jiang, D.; Zhao, H.; Zhang, S.; John, R. *J. Phys. Chem. B* **2003**, *107*, 12774–12780.

(30) Lightcap, I. V.; Kosel, T. H.; Kamat, P. V. *Nano Lett.* **2010**, *10*, 577–583.

(31) Meyer, T. J.; Meyer, G. J.; Pfennig, B. W.; Schoonover, J. R.; Timpson, C. J.; Wall, J. F.; Kobusch, C.; Chen, X. H.; Peek, B. M. *Inorg. Chem.* **1994**, *33*, 3952–3964.

(32) McAllister, M. J.; Li, J.-L.; Adamson, D. H.; Schniepp, H. C.; Abdala, A. A.; Liu, J.; Herrera-Alonso, M.; Milius, D. L.; Car, R.; Prud'homme, R. K.; Aksay, I. A. *Chem. Mater.* **2007**, *19*, 4396–4404.

(33) Moon, I. K.; Lee, J.; Ruoff, R. S.; Lee, H. *Nat. Commun.* **2010**, *1*, 73.

(34) Fan, Y.; Lu, H. T.; Liu, J. H.; Yang, C. P.; Jing, Q. S.; Zhang, Y. X.; Yang, X. K.; Huang, K. *J. Colloids Surf., B* **2011**, *83*, 78–82.

(35) Zhang, H.; Fan, X.; Quan, X.; Chen, S.; Yu, H. *Environ. Sci. Technol.* **2011**, *45*, 5731–5736.

(36) Li, N.; Liu, G.; Zhen, C.; Li, F.; Zhang, L.; Cheng, H.-M. *Adv. Funct. Mater.* **2011**, *21*, 1717–1722.

(37) Falaras, P.; Hugot-Le Goff, A.; Bernard, M. C.; Xagas, A. *Sol. Energy Mater. Sol. Cells* **2000**, *64*, 167–184.

(38) Zhang, W. L.; Liu, Y. D.; Choi, H. J.; Kim, S. G. *ACS Appl. Mater. Interfaces* **2012**, *4*, 2267–2272.

(39) Lindstrom, H.; Södergren, S.; Solbrand, A.; Rensmo, H.; Hjelm, J.; Hagfeldt, A.; Lindquist, S.-E. *J. Phys. Chem. B* **1997**, *101*, 7717–7722.

(40) van de Krol, R.; Goossens, A.; Meulenkamp, E. A. *J. Electrochem. Soc.* **1999**, *146*, 3150–3154.

(41) Zhu, X.; Zhu, Y.; Murali, S.; Stoller, M. D.; Ruoff, R. S. *ACS Nano* **2011**, *5*, 3333–3338.

(42) Ding, Y.-H.; Zhang, P.; Ren, H.-M.; Zhuo, Q.; Yang, Z.-M.; Jiang, Y. *Mater. Res. Bull.* **2011**, *46*, 2403–2407.

(43) Cao, H.; Li, B.; Zhang, J.; Lian, F.; Kong, X.; Qu, M. *J. Mater. Chem.* **2012**, *22*, 9759–9766.

(44) Bueno, P. R.; Leite, E. R. *J. Phys. Chem. B* **2003**, *107*, 8868–8877.